J. Plasma Phys. (2024), *vol*. 90, 905900413
Published by Cambridge University Press
doi:10.1017/S0022377824000758

Self-consistent effects in the ponderomotive acceleration of electron beams

I. Almansa [1], F. Russman [1], E. Peter [1], S. Marini [2,†] and F.B. Rizzato [1]

[1]Instituto de Física, Universidade Federal do Rio Grande do Sul, Caixa Postal 15051, 91501-970 Porto Alegre, RS, Brasil

[2]CEA, IRFU, DACM, Université Paris-Saclay, 91191 Gif-sur-Yvette, France

(Received 29 November 2023; revised 22 May 2024; accepted 23 May 2024)

In the present work, we extend the results of a previous investigation on the dynamics of electrons under the action of an inverse free-electron-laser scheme (Almansa *et al.*, *Phys. Plasmas*, vol. 26, 2019, 033105). While the former work examined electrons as single test particles subject to the combined action of a modulated wiggler plus a laser field, we now look at electrons as composing a particle beam, where collective space-charge effects are relevant and included in the analysis. Our previous work showed that effective acceleration is achieved when the initial velocities of the particles are close enough to the phase velocity of the beat-wave mode formed by the laser and the wiggler fields. Electrons are then initially accelerated by a ponderomotive uphill effect generated by the beat mode and, once reaching the phase velocity of the beat, undergo a final strong resonant acceleration step resembling a catapult effect. The present work shows that, under proper conditions, space-charge effects play a similar role as the initial (or injected) velocity of the beam. Even if acceleration is absent when space charge is neglected, it may be present and effective when charge effects are taken into account. We also discuss how far the space charge can grow without affecting the sustainability of the acceleration process.

Keywords: plasma simulation, plasma dynamics, intense particle beams

1. Introduction

Recent results show that efficient electron acceleration can be achieved as one combines an inverse free-electron-laser (IFEL) scheme (Courant, Pellegrini & Zakowicz 1985; van Steenbergen *et al.* 1996; Ho *et al.* 2013; Duris *et al.* 2014; Singh *et al.* 2022) with a preceding ponderomotive (Shukla *et al.* 1986; Mendonça 2001; Macchi 2013) step, both stages formed with the very same laser and static wiggler fields (Almansa *et al.* 2019). The ponderomotive stage requires a wiggler whose amplitude is modulated along the device's axial direction, defined by the co-aligned orientation of both wiggler and laser wave vectors.

As electrons are injected, the non-uniform wiggler enables pre-acceleration by means of an uphill effective ponderomotive potential (Mulser & Bauer 2010; Burton *et al.* 2017; Ruiz & Dodin 2017; Almansa *et al.* 2018). Electrons are then resonantly pushed forward by the peaks of the beat wave formed by laser and wiggler, and ultimately accelerated in

† Email address for correspondence: marini_samuel@yahoo.com.br

a catapult fashion to higher velocities than the phase velocity of the beat wave and much higher final energies than the initial. We note that the non-uniform shape of the wiggler both promotes acceleration and allows particles to escape at the far end of the accelerating region. These features contrast with the case of uniform fields where particles remain trapped – undergoing a mixing process – once they fall into the field's troughs (Evstatiev, Morrison & Horton 2005).

As an initial approach, especially if the complexities of the ponderomotive uphill acceleration are considered, one disregards collective effects involving the accelerating electrons and the concomitant back reaction of these particles on the original electromagnetic fields. This is justified if one works with a rarefied electron population, which under these circumstances behaves as a test particle conglomerate.

On the other hand, if one thinks of relatively high-density beams used, for instance, in material processing devices (Davidson & Qin 2001), collective self-consistent effects should be considered.

The purpose of the present analysis is precisely to add collective effects to the description of electron acceleration in the IFEL device described above.

The transverse self-consistent beam dynamics has been largely analysed and understood when beams are transported at constant axial speeds in the absence of accelerating fields. In the present case, we need to take into account the presence of driving non-uniform electromagnetic fields along the axial direction, as commented above. The beam will still be transported along the axis but with varying velocity and density resulting from its non-homogeneous longitudinal profile. Therefore, the theory for uniform transport along the axial direction shall be adapted accordingly to describe how acceleration, collective effects and non-uniform transport relate to each other.

In the following sections, we will introduce the laser and wiggler fields, focusing on their respective polarizations and profiles along the axial direction of the IFEL device. With the rapidly varying fields duly introduced and now adding the slowly varying space-charge collective fields, we shall develop the proper ponderomotive Hamiltonian describing the averaged electron dynamics. In the final step, we solve the self-consistent collective system formed by particles and fields and compare the results with the dynamics of test particles moving under the same circumstances.

The overall analysis is carried out under the assumption that the smooth ponderomotive averaged dynamics is stationary, depending only on the longitudinal and transverse spatial coordinates of a cylindrical geometry.

2. General formalism

2.1. *Laser and wiggler fields*

As mentioned in the Introduction and discussed in Almansa *et al.* (2019), the acceleration scheme investigated here depends on the combination of laser and wiggler fields in an IFEL device arrangement where electrons draw energy from a pre-existing finite-amplitude laser mode. We consider the focal region of the electromagnetic fields to be sufficiently larger than the beam radius, so that we can discard transverse features in both the wiggler and the laser. Dissipative forces, like radiation reaction, are in general comparatively small and also neglected here (Landau & Lifschitz 1965; Vranic *et al.* 2014; Russman, Marini & Rizzato 2022).

In the static wiggler case, the uniformity condition on transverse dimensions has been discussed in more detail in Almansa *et al.* (2019) and allows us to take the respective vector

https://doi.org/10.1017/S0022377824000758 Published online by Cambridge University Press

potential field $\boldsymbol{A}_w$ in the form of a right-handed circularly polarized mode

$$\boldsymbol{A}_w = A_{w0}\,\mathrm{e}^{-(x^2/\sigma^2)}\frac{\hat{\boldsymbol{y}}+\mathrm{i}\hat{\boldsymbol{z}}}{2}\mathrm{e}^{\mathrm{i}\theta_w} + \mathrm{c.c.}, \tag{2.1}$$

where A_{w0} represents the peak amplitude of a slowly modulated wiggler displaying a rapidly varying phase $\theta_w = k_w x$; one enforces the slow modulation condition demanding $k_w\sigma \gg 1$, with k_w as the wiggler wave vector and 2σ as its extension around $x = 0$.

As for the dynamical laser field $\boldsymbol{A}_l(x)$, we will not only require an initially large cross-section, but also that its cross-section remains mostly unchanged along the axial direction. This requirement is equivalent to excluding transverse laser beam expansion, therefore holding constant the laser intensity at the central alignment of the system (Elmore, Elmore & Heald 1985). Introducing $\sigma_{\perp\mathrm{laser}}$ as the laser cross-sectional radial dimension, L as the system longitudinal length and k_l as the laser wavevector then, in the absence of dissipative forces involving the laser particle interaction, one can use the slowly modulated wave equation for the laser to show that, if $L \ll k_l\sigma^2_{\perp\mathrm{laser}}$, the laser beam does not appreciably expand transversely. One should also require $L > \sigma_{\perp\mathrm{laser}}$ to enforce a beam geometry for the laser, from which follows the expected necessary condition $k_l\sigma_{\perp\mathrm{laser}} \gg 1$ indicating that the cross-sectional dimension should be much larger than the laser wavelength.

Working with a left-handed polarized signal, the above set of conditions allows us to write

$$\boldsymbol{A}_l(x,t) = A_{l0}\frac{\hat{\boldsymbol{y}}-\mathrm{i}\hat{\boldsymbol{z}}}{2}\mathrm{e}^{\mathrm{i}\theta_l} + \mathrm{c.c.}, \tag{2.2}$$

with the laser amplitude constant and the fast phase written in the form $\theta_l \equiv k_l x - \omega_l t + \phi_{\mathrm{slow}}(x)$. We shall consider a sufficiently underdense electron beam such that $\omega_l/k_l \approx c$, with ω_l as the laser fast frequency and c as the speed of light. The added slowly varying phase correction ϕ_{slow} due to the beam's presence can be neglected.

2.2. *Collective fields*

Let us finally discuss the presence and actions of space-charge collective fields in our model. This is a new feature which is non-existent in the previous single-particle view, where collective effects are absent and where the only low-frequency field results from the ponderomotive action of the laser and wiggler fields preceding the catapulting acceleration discussed earlier.

In our case, we consider a continuous dense particle beam with cylindrical symmetry, where collective low-frequency space-charge fields are generated due to particle–particle interaction.

The primary low-frequency collective field to be considered is the space-charge potential. This low-frequency collective mode has an axial and, importantly, a transverse dependency resulting from the interplay between the finite cross-sectional area of the beam and the boundary conditions surrounding the system. The space-charge potential is denoted by

$$\varphi = \varphi(r,x), \tag{2.3}$$

where we recall the assumed cylindrical geometry characterized by the absence of the azimuthal angle. We shall also consider a thin beam configuration for which the aspect ratio $|\nabla_\perp| \gg |\partial/\partial x|$ applies, so the potential can be obtained from a purely transverse

https://doi.org/10.1017/S0022377824000758 Published online by Cambridge University Press

form of the Poisson equation

$$\nabla_{\perp}^{2}\varphi = -qn/\epsilon_0, \tag{2.4}$$

with x seen as a parametric variable, ϵ_0 as the vacuum permittivity, q as the particle's charge and $n = n(x, r)$ as the beam density which will be detailed shortly.

We also observe that the thin beam geometrical aspect remains valid while the displacement of any beam particle along the longitudinal axis x corresponds to a much smaller transverse displacement. This condition, in general, requires high axial relativistic speeds which alone could be sufficient to validate the use of the Poisson equation in its transverse form (Vay 2008; Londrillo, Gatti & Ferrario 2014).

For the given beam density, (2.4) will be solved under the boundary condition $\varphi(x, r = r_w) = 0$, where r_w denotes the radius of a conducting wall surrounding the system, which is sufficiently larger than the beam dimensions.

For the purposes of the present investigation, we shall take beams of homogeneous density and sharply defined slowly varying boundary at $r_b = r_b(x)$, a pair of assumptions that will be justified shortly.

Under these conditions, and recalling the restriction to stationary dynamical regimes, the following expression can be obtained for the beam density at any point along the axial direction:

$$n(x) = \frac{Q_0}{\pi r_b(x)^2 v_x(x)}, \tag{2.5}$$

where $Q_0 \equiv \pi r_b(0)^2 n(0) v_x(0)$ measures the unnormalized injected charge flow at $x = 0$, and where we introduce the slowly varying axial beam velocity v_x which will be taken as approximately constant over any transverse area of the thin beam. Note that the electron flow, as defined by Q_0, implies a smooth, steady-state particle inflow at the beam injection point.

Along the longitudinal axis, however, the density must undergo any necessary changes in order to preserve the constant current flow. With this adjustment, for a given set $Q_0, r_b(x), v_x(x)$, the resulting transversely homogeneous beam density, obtained from expression (2.5), can be inserted in the Poisson equation (2.4), whose solution provides the potential φ acting on any point along and across the beam in the form

$$\varphi(x, r \le r_b(x)) = \frac{v_\phi^2 Q_0}{4\pi v_x(x)} \left(1 + 2\ln\left(\frac{r_w}{r_b(x)}\right) - \frac{r^2}{r_b(x)^2}\right), \tag{2.6}$$

where v_ϕ is the carrier phase velocity. From now on, we progressively switch the formalism to dimensionless variables, starting with $(k_w + k_l)(x, y, z) \to (x, y, z)$, $(k_w + k_l)ct \to t, q\varphi/mc^2 \to \varphi$ and $n/n_c \to n$ (where m is the particle mass). Speeds are therefore normalized by the speed of light; in particular, the normalized carrier phase velocity reads $k_l/(k_w + k_l)$. Moreover, n_c is introduced as the critical density for wave propagation in the beam: $n_c = \epsilon_0 m\omega_l^2/q^2$. We use n_c as a convenient parameter to fully render Q_0 seen in expression (2.5) into a non-dimensional form.

Note that, since the beam may have a considerable velocity along the axial coordinate, a closely related field to φ should be introduced: the axial component of the vector potential, A_x. In contrast to the vector potentials connected to the laser and wiggler fields, A_x is a slowly varying field with its source arising from the equally slowly varying axial current density $j_x = qnv_x$.

https://doi.org/10.1017/S0022377824000758 Published online by Cambridge University Press

From the same stationary thin beam assumptions, now, along with the wave equation for the vector potential and with expression (2.6), one obtains

$$\nabla_\perp^2 A_x = -q\mu_0 n v_x = \nabla_\perp^2 \varphi v_x/c^2, \tag{2.7}$$

where μ_0 is the vacuum permeability. Equation (2.7) translates into the non-dimensional form as

$$A_x = \varphi v_x, \tag{2.8}$$

with $qA_x/mc \to A_x$, similarly as discussed in Davidson & Qin (2001), and we apply the same normalization condition to the laser and wiggler fields to obtain the overall rule $q\boldsymbol{A}/mc \to \boldsymbol{A}$ for the vector potential.

Examining expressions (2.6) and (2.8) we thus see that, under the present assumptions, the slowly varying beam potentials – and the beam itself – are entirely characterized and governed by the variable beam speed and variable beam radius. Our next step is to work out the appropriate self-consistent dynamical equations that will allow us to calculate these quantities.

2.3. *Particle and beam dynamics*

Now that we have an initial sketch for the basic structure of the EM fields, we proceed to the next step, where the particle and beam dynamics are investigated. This section establishes the theoretical framework essential for the numerical simulations presented in the following section.

Particles are subjected to the action of the rapidly varying laser ($\boldsymbol{A}_l$) and wiggler ($\boldsymbol{A}_w$), alongside the space-charge related fields φ and A_x self-consistently acting upon the whole beam.

We start by looking into the dynamics of a particle with canonical momentum $\boldsymbol{p}$ with the help of the respective dimensionless Hamiltonian ($H/mc^2 \to H$)

$$H = \sqrt{1 + (\boldsymbol{p} - \boldsymbol{A})^2} + \varphi, \tag{2.9}$$

where $\boldsymbol{A} = \boldsymbol{A}_l + \boldsymbol{A}_w + A_x\hat{\boldsymbol{x}}$.

As discussed earlier, potentials φ and A_x appearing in expression (2.9) do not depend on the fast phases $\theta_{l,w}$ and in this sense are thus slowly varying functions of axial and transverse coordinates. Since we are considering a narrow beam which essentially sees plane electromagnetic waves aligned with the axis, we conclude, from the Hamiltonian equation $\dot{\boldsymbol{p}}_\perp = -\boldsymbol{\nabla}_\perp H$, that $\boldsymbol{p}_\perp$ is a slowly varying coordinate as well.

Our interest is to proceed further in the quest for a fully averaged Hamiltonian capable of describing the ponderomotive dynamics leading to particle trapping and the ultimate resonant – or catapult – acceleration, as commented earlier. We will also see that the averaged variables obtained from the ponderomotive procedure are of central importance to constructing the slowly varying self-consistent fields acting on the particles.

In order to obtain the average form, we proceed along the ensuing general lines.

We shall first recall that although the transverse momentum $\boldsymbol{p}_\perp$ is a slowly varying variable, neither the full Hamiltonian H nor the axial momentum p_x are – a fact resulting from the presence of the fast varying phases θ_l and θ_w in the canonical dynamics. For a generic variable g we thus write

$$g = \bar{g} + \delta g, \tag{2.10}$$

where $\bar{g}$ represent the fast phase average of g, and δg represents the rapidly varying fluctuations of g due to the presence of the fast phases.

https://doi.org/10.1017/S0022377824000758 Published online by Cambridge University Press

We then shift the scalar potential to the left-hand side of expression (2.9), take the square of both sides of the resulting equality and write all variables in the form (2.10), observing that $\overline{\delta g} = 0$.

The final result can be cast as

$$\bar{H} = \sqrt{1 + (\bar{p}_x - A_x)^2 + \boldsymbol{p}_\perp^2 + \overline{(\delta p_x)^2} - \overline{(\delta H)^2} + A_{l0}^2 + A_w^2(x)} + \varphi, \tag{2.11}$$

where we point out the presence of the averaged quadratic fluctuations related to the axial momentum and to the Hamiltonian itself. Both are crucial for the full description of the dynamics, and we see that, in addition, we will indeed need the vector potential A_x along the $x-$axis and the space-charge potential φ, which can be calculated from (2.4) and (2.7), respectively.

Calculation of the fluctuations terms δp_x and δH are based on the canonical integration of Hamiltonian (2.9) over the fast time scales dictated by wave frequencies and wave vectors, with slow variables kept fixed. The procedure is long and deferred to Appendix A.

The various steps leading to the average Hamiltonian emerge in Appendix, and in the conveniently approximated expression (B2)

$$\bar{H}_{\text{approx}} \equiv H_0 + H_2, \tag{2.12}$$

which is reached if one uses the assumption that the energy associated with the longitudinal motion is much larger than the one associated with the transverse dynamics. In practice, we shall assume $\bar{p}_x \gg \varphi, |\boldsymbol{p}_\perp|$ in dimensionless forms, and expand the full $\bar{H}$ up to quadratic terms in r and $\boldsymbol{p}_\perp$. Here, H_0 does not contain r and $\boldsymbol{p}_\perp$, and H_2 is quadratic in both variables. We point out that it is precisely the quadratic dependence of $\bar{H}_{\text{approx}}$ on r that allows the use of transversely homogeneous beams as required by expressions (2.5) and (2.6). Spatially quadratic potentials generate spatially linear forces that, in turn, sustain uniformity in the geometry analysed here (Davidson & Qin 2001).

In addition, the energetic contribution of H_2 to the full Hamiltonian is closely related to the potential term proportional to Q_0, as seen in (B5) of Appendix B. In this context, to maintain consistency with our initial assumptions of a thin beam geometry resulting from velocities along the axis being greater than velocities transverse to the axis, we shall therefore consider limited values for Q_0, which is the condition discussed earlier in the context of (2.4). This condition is further discussed following expression (B5).

We next suppress the overbar on average quantities in order to ease off the notation, and solve the dynamics that arises from Hamiltonian (2.12) under a stationary regime, as stated earlier, in two steps. We first focus on the zeroth-order contribution to H_{approx}, $H_0(x, p_x)$, with φ to be calculated from expression (2.6) at $r = 0$. From this zeroth order we readily obtain the canonical pair of equations

$$\mathrm{d}p_x/\mathrm{d}x = (1/v_x)\,\mathrm{d}p_x/\mathrm{d}t = -(1/v_x)\partial H_0/\partial x, \tag{2.13}$$

$$v_x = \mathrm{d}x/\mathrm{d}t = \partial H_0/\partial p_x, \tag{2.14}$$

eventually leading to a radially independent expression for $v_x = v_x(x)$, which we will thus take as our approximation for the beam velocity.

We see, however, that, in order to accomplish the calculation of v_x, we need expressions for $\mathrm{d}v_x/\mathrm{d}x$ and $\mathrm{d}r_b/\mathrm{d}x$ as well, since both arise from the space derivative $\partial\varphi/\partial x$ present in $\partial H_0/\partial x$ of (2.13).

A derivation of $\mathrm{d}v_x/\mathrm{d}x$ from v_x in (2.14) is straightforward, despite its lengthiness. To calculate $\mathrm{d}r_b/\mathrm{d}x$, which appears in (2.13) as well as in $\mathrm{d}v_x/\mathrm{d}x$, we need, however, to make

https://doi.org/10.1017/S0022377824000758 Published online by Cambridge University Press

use of the second term of H_{approx}, H_2, quadratic in the canonical variables r and p_r. The strategy is to obtain the canonical equations for $\mathrm{d}r/\mathrm{d}x$ and $\mathrm{d}p_r/\mathrm{d}x$ and evaluate both at $r = r_b$ and $p = p_b$, with 'b' designating the beam boundary.

All in all, we need to numerically solve a system of four coupled dynamical differential equations: one for $p_x(x)$, one for $v_x(x)$, one for $r_b(x)$ and, finally, one for $p_b(x)$. We refer to this procedure as the ponderomotive approach to the problem. We point out that the ponderomotive approach results in the simultaneous calculation of both the longitudinal speed of the beam and the beam envelope (one cannot calculate one without calculating the other). Under the ponderomotive approximation, all particles have the same longitudinal velocity and are surrounded by the common smooth envelope of radius r_b.

As soon as the slowly varying potentials φ and A_x are obtained in terms of v_x and r_b as in (2.6), we shall proceed to the next step where we relax the ponderomotive approximations involving the effects of laser and wiggler fields on the beam particles. At this point, we can compare the exact dynamics with the averaged ponderomotive approximation, as well as investigate the strong resonant acceleration as particles fall into the troughs formed by the beating of wiggler and laser. In all instances, the role of space charges can be duly identified and analysed.

It should be understood that, when the exact dynamics of single particles deviates from the corresponding ponderomotive approximation, the very idea of a smooth beam is to be taken with caution. We will examine this issue and argue that the smooth beam model is still useful even when acceleration regime due to particle trapping and kicking starts to set in.

3. Numerical analysis

The clearest role of space-charge effects is arguably in the beam's cross-sectional spread along the longitudinal axis. In the absence of any collective effects, the beam reverts to a collection of non-interacting test particles that can even be longitudinally accelerated while still preserving the initial transverse dynamics. As one 'turns on' the charge parameter Q_0, collective effects and beam spread should be seen.

To discuss the effects of space charge addressed in previous sections, we fix a set of parameters with both the laser field and wiggler amplitudes given by $A_{l,0} = A_{w,0} = 1.2$, (indicative of a moderately relativistic regime of interaction), $\sigma = 100$, $v_\phi = \sqrt{0.9}$, $v_y(0) = v_z(0) = 0$, $x(0) = -10\sigma$ and $r_w = 150$. We consider the parameters $r(0)$, $v_x(0)$, and $Q(0) \equiv Q_0$ as free variables to explore the main effects arising from space charge.

In figure 1, we examine a geometrical cut across the beam longitudinal midplane to examine the evolution of the upper and lowermost points of the beam envelope along the longitudinal axis x. Discrete choices for the initial beam radii and charges are made, and we keep the initial velocity constant at $v_x(0) = 0.86$. The dashed blue line represents $Q_0 = 0.001$ in both panels, and the solid red line likewise represents $Q_0 = 0.06$. Note that, for a better insight into the beam's dynamics and geometry, we represent the beam radius growth symmetrically as the beam uniformly expands.

When the initial radius equals $r_b(0) = 30$, as shown in panel (a), we can see that if the charge is small, the opening of the beam radius is also small, as expected. However, when the initial charge is relatively large, we observe a significant variation in the beam radius, which at the end of the interaction, with $x \approx 1000$, has a final radius measuring approximately $r_b(x_f) = 90$; 3 times its initial size.

As one increases the initial beam radius, the charge becomes distributed over a larger cross-sectional area, which results in less significant space-charge effects than in the previous case. Indeed, when $Q_0 = 0.001$, there is virtually no variation in the particles'

https://doi.org/10.1017/S0022377824000758 Published online by Cambridge University Press

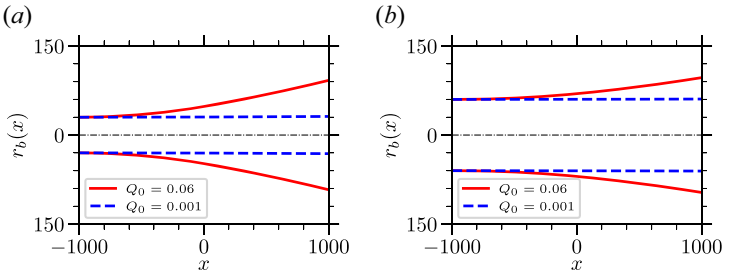

FIGURE 1. Envelope evolution in the x direction as a function of initial charge flow $Q_0 = 0.001$ (dashed blue line) and $Q_0 = 0.06$ (solid red line), initial velocity $v_x(0) = 0.86$ and with radii $r(0) = 30$ (a) and $r(0) = 60$ (b).

radii, and when $Q_0 = 0.06$ the beam still expands up to an observable larger radius $r_b(x_f) = 90$, but with this latter value now representing only a small incremental fraction of its initial size.

Looking at the longitudinal and transverse scales, we point out that the beam envelope smoothly evolves in a much slower rate than it advances along the longitudinal axis, which corroborates the thin beam approach promulgated earlier. We note that not even the length scale associated with the wiggler field's envelope affects the ponderomotive dynamics as particles run through the region $x \sim 0$ with relativistic speeds.

To better understand the effects of both electromagnetic and space-charge fields, a number of individual particles obeying the full dynamics dictated by the newly considered collective effects plus the full wiggler and laser fields can also be included in the simulations. As commented earlier, we deem the ponderomotive approximation to be correct as long as the test particle orbits agree with their averaged counterpart.

A collection of 60 test particles is randomly but uniformly distributed over the initial respective cross-sectional area on the plane (y, z), and their dynamics is henceforth described by the full Hamiltonian (2.9). To mimic the symmetry seen in figure 1, particles launched in the lower (upper) quadrants of the plane (y, z) are represented below (above) the $r_b = 0$ axis. Figure 2 reveals how the various radial orbits of the particles evolve along the axis. The various grey curves represent regularly expanding orbits, solid red curves represent beam boundaries and the purple curve represents the central orbit. The sinuous orbits (seen in panel figure 2(e) and discussed below) are represented in blue. We set $r_b(0) = 60$ and $v_x(0) = 0.86$, with $Q_0 = 0.001$ in panels (a,b), $Q_0 = 0.06$ in panels (c,d) and $Q_0 = 0.12$ in panels (e,f).

In panel (a), we can observe that the test particles flow homogeneously within the region bounded by an approximately constant envelope. The slight inter-crossings of particle trajectories seen are due to the high-frequency jitter driven by the laser and wiggler fields and does not affect our model for the smooth collective space-charge fields.

Complementarily, in panel (b) we refer to the time history of all test particles' respective velocities, including the central particle – we call them v_x^{test} – which again reveals the uphill acceleration. Translating the highly oscillating exact velocity v_x^{test} into its time average form, one can see either from our previous work (Almansa *et al.* 2019), or from the green curve representing the average velocity, that the latter closely follows the upper envelope of the exact v_x^{test}, with a slightly more pronounced dip at $x = 0$. The dip is, however, much less profound than the one associated with the exact velocities v_x^{test}, which keeps v_x well above the breakup level $v_x = 0$, an essential ingredient for thin beam modelling. Particles are accelerated as they enter the region of the first peak in panel (b),

https://doi.org/10.1017/S0022377824000758 Published online by Cambridge University Press

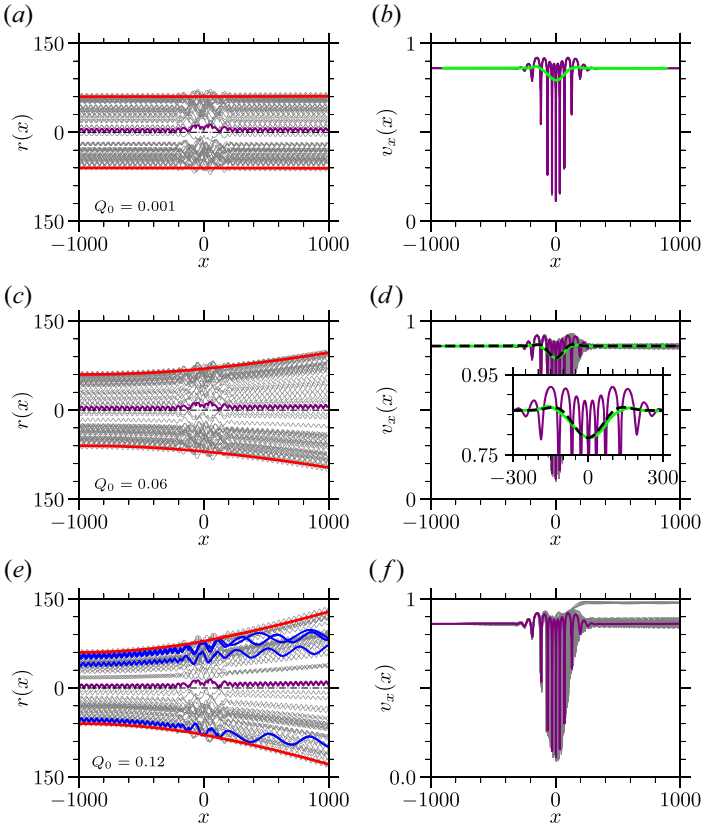

FIGURE 2. Case of $Q_0 = 0.001$ in (*a*,*b*), $Q_0 = 0.06$ in (*c*,*d*) and $Q_0 = 0.12$ in (*e*,*f*); here, $v_{x0} = 0.86$ and v_x on the vertical axes represents both the test particles' velocities and the ponderomotive velocities, obtained from averaging over fast oscillations (green curve) and from (2.12) (black dashed curve). The envelope of the beam is depicted in red. Regular grey curves in the spatial panels $r(x) \times x$ depict the uniformly expanding, non-catapulting beam particles. In contrast, the sinuous blue curves appearing in panel (*e*) represent the catapulted, highly accelerated particles observed on the right upper side of panel (*f*).

decelerated as they approach the coordinate $x = 0$, accelerated again near the second peak and decelerated once more to be finally ejected with the very same initial velocity.

At these lowest levels of space charge, and for the considered injection velocity, the overall conclusion is that the beam behaves as in the previously studied case (Almansa *et al.* 2019) where the particle motion is mostly aligned with the longitudinal axis and the final catapulting acceleration is totally absent.

In panel (*c*) we can now observe the particle flow evolution when the initial charge is significantly larger, with $Q_0 = 0.06$. Notwithstanding the more substantial charge value leading to a final envelope twice as large as the previous one, the flow is still homogeneous, and our initial assumptions are once again corroborated. In addition, we note from panel (*d*) that all particles are approximately co-moving with the very same velocity, which again advocates in favour of a unique value for the beam velocity, even for the larger Q_0. We also note the presence of the uphill acceleration but the absence of the catapulting dynamics. Thus, at this level of the charge factor Q_0, the transverse dynamics already exhibits the action of collective effects, but the forward dynamics remains unaffected. Also

https://doi.org/10.1017/S0022377824000758 Published online by Cambridge University Press

in panel (*d*) we add an inset for this case of a larger Q_0. The green curve is derived from averaging the rapid oscillations of a test particle's velocity at $r = 0$ while the dashed black line directly results from integrating the equations derived from the Hamiltonian given by (2.12). The agreement of the ponderomotive approximation and the time averaging is still solid. In addition, the corresponding panel (*c*) reveals that, under the same regime, the radius r_b obtained from the ponderomotive approach agrees very well with the exact radial dynamics of test particles launched at the beam border, which can also be seen as an important feature validating the theory.

Then, as we move to panels (*e*,*f*), the even larger space-charge effects for $Q_0 = 0.12$ not only further expand the beam envelope but introduce the catapulting dynamics as well. We just recall that, in the absence of space-charge effects (Almansa *et al.* 2019), the catapult acceleration was solely driven by the velocity of the injected particles, which panel (*a*) shows to be insufficient in this case. We thus see that the charge flow parameter Q_0 is also a determining factor for acceleration.

We then argue that those particles near the beam border are the first ones to undergo the acceleration process. The background beam core remains largely unaffected, orbits remain dominantly homogeneous without inter-crossing and the beam velocity is dominantly the same for the whole beam. This is a peculiar regime where one can examine the orbits of individual accelerating particles, still using with confidence our collective model to represent the self-consistent space-charge effects.

In fact, with the collective model we can examine the dynamics as a function of the beam radial coordinate, looking at the r-dependent terms of H_2 in expression (2.12), let us call it H_{2r}

$$H_{2r} = \frac{Q_0 r^2(x)}{r_b^2(x)} \frac{(1 - v_x^2(x))}{v_x(x)}. \tag{3.1}$$

From the expression above, we can see that H_{2r} becomes more significant near the beam's largest radii. From a perturbative expansion point of view, let us then examine the role of H_{2r} for particles precisely at the border $r(x) = r_b(x)$. We consider a beam of particles moving forward with a velocity $v_x > 0$, which must be less than unity as it is normalized to the speed of light. If the uphill acceleration is present, even if small, as v_x tries to reach higher speeds at any of the two peaks seen in the velocity plots of figure 2(*b*) for instance (Almansa *et al.* 2019), the 'potential energy' H_{2r} starts to act as its own magnitude decreases, delivering a forward extra kick proportional to Q_0 that helps to pull particles into resonance with the beat mode formed by laser and wiggler. This is seen in figure 2(*f*) as the clearly distinct group of highly accelerated particles with speeds close to c, whose no longer homogeneous spatial orbits correspond to the highly sinuous curves near the boundary at $r_b(x)$, visible as the blue curves in panel (*e*).

On the other hand, if the uphill acceleration is not significant, typically for lower injection velocities, the downhill valley seen in figure 2 decreases v_x, augments, therefore, H_2 and may even reflect particles backward. This is precisely what is seen in figure 3. The beam's central body continues to move forward after $x = 0$, but some of the particles are already seen moving backward. It is important to emphasize that in the absence of space-charge effects with $Q_0 \to 0$, the whole beam would keep moving forward. This last case of figure 3 should be seen with reserve since, although Q_0 is small, the longitudinal speeds are originally smaller too. These conditions break the beam's longitudinal smoothness at $x = 0$ and put us on the verge of the validity of our thin beam approximations, but nevertheless provide a first approach to the case where reflection is present. We also point out that r_w in figure 3(*a*) was expanded to $r_w = 5000$ in order to

https://doi.org/10.1017/S0022377824000758 Published online by Cambridge University Press

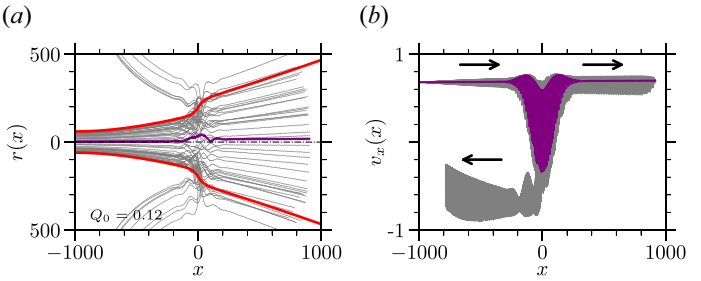

FIGURE 3. Case of $Q_0 = 0.12$ and $v_{x0} = 0.68$. (*a*) Evolution of test particle trajectories with the red curves representing the evolution of the beam envelope, and (*b*) evolution of test particle velocities. In both panels, test particles are depicted in grey, with the purple curve denoting the central particle at $r(x) \approx 0$. Black arrows in (*b*) indicate the direction the particles are moving in.

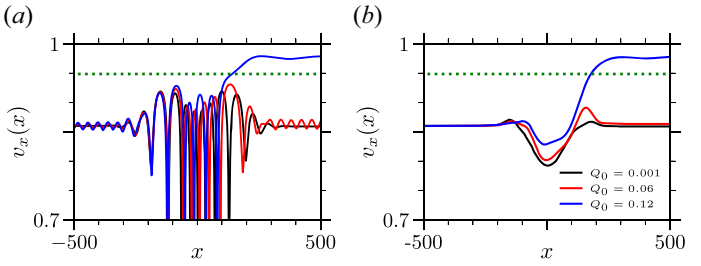

FIGURE 4. Time evolution of velocity for particles at the border of the beam distribution assuming different initial charge flows. Panel (*a*) shows the full velocity, and panel (*b*) depicts the averaging over the rapid oscillations observed in the test particle's velocity. In both panels, the dotted green line represents the carrier phase velocity. The figures demonstrate that, for higher charge flow, the final velocity of the test particle changes from unperturbed at $Q_0 = 0.001$ (black curve) to perturbed at $Q_0 = 0.06$ (red curve) and finally to accelerated at $Q_0 = 0.12$ (blue curve).

accommodate the beam; the expansion of the conducting wall radius has very little effect on the dynamics since the potentials depend only logarithmically on r_w.

In summary, the H_2 term contributes a forward extra kick if the uphill acceleration is present and a backward extra kick if the uphill acceleration is negligible.

We examine the charge flow effect on particles at the border of the beam distribution looking at their velocity evolution, as depicted in figure 4. Panel (*a*) shows the full temporal evolution and panel (*b*) the corresponding time average. The time average equals the ponderomotive description if one is far enough from the resonance. The figure shows that, when the beam charge flow is low or near zero, i.e. $Q_0 = 0.001$, the final velocity of the particle remains unchanged from its initial state, as indicated by the solid black curve. However, for a charge flow of $Q_0 = 0.06$ (red curve), particles at the border experience a significant increment in velocity as they traverse the region where the wiggler field is intense, as predicted by (3.1). However, the increment is not large enough to bring the particle into resonance with the carrier beat wave and the particle eventually returns to its initial state. For a charge flow of $Q_0 = 0.12$ (blue curve), the space charge is finally strong enough to accelerate some particle into resonance, from which point they are strongly kicked and further accelerated by the beat wave.

In figure 5, we examine a particle beam with an initial radius $r_0 = 60$ and different initial velocities, $v_{x0} = 0.82$, 0.84 and 0.86, depicted by the green squares, blue triangles

https://doi.org/10.1017/S0022377824000758 Published online by Cambridge University Press

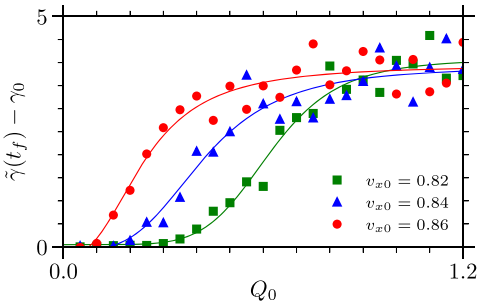

FIGURE 5. Saturation of energy gain as a function of initial beam velocity. Green squares, blue triangles and red dots represent particles with initial velocities $v_{x0} = 0.82$, $v_{x0} = 0.84$ and $v_{x0} = 0.86$, respectively. Solid curves are fitting curves to guide the eye.

and red points, respectively. In the figure, the energy gain, denoted as $\tilde{\gamma}(t_f) - \gamma_0$, is plotted against the initial charge Q_0, where the mean energy, $\tilde{\gamma}$, at the final time $t = t_f$ is defined as $\tilde{\gamma}(t_f) = (1/n) \sum_{i=1}^{n} \gamma_i(t_f)$. The figure shows that the energy gain tends to saturate as one increases the initial charge. Saturation occurs at different points for each initial velocity: for $v_{x0} = 0.86$, saturation occurs approximately at $Q_0 = 0.4$, for $v_{x0} = 0.84$ at $Q_0 = 0.6$ and for $v_{x0} = 0.84$, saturation is only observed for larger charges above $Q_0 = 1.2$.

The saturation behaviour is attributed to a shifting position of the resonant particle group as the initial charge escalates. At zero charge, no resonance is present under the present circumstances. However, as Q_0 grows, at a certain point particles on the beam border r_b are first kicked with the exact amount of energy into resonance, which results from the fact that the kick's amplitude, proportional to r^2, is the most intense at the border. This is the case previously discussed along with figure 2(f).

From this point on, as Q_0 keeps growing the resonance locus plunges deeper towards the central region of the beam in order to preserve the extra-kick amplitude given by the product $Q_0 r^2$. In this cyclic behaviour, as a new group of particles goes into resonance, the previous adjacent group falls off resonance. This interchange between limited resonant particle groups explains the complex dynamics manifested in the figure. In particular, it explains why the energy gain remains the same once installed; the carriers of the energy gain change in position but not in number.

The solid curves represent fitting curves to guide the eye. Fluctuations in the values are related to the particle's initial position, which, in turn, is determined randomly.

4. Conclusions

In the present paper, we studied the role of self-consistent space-charge effects on the acceleration of particle beams under the external action of laser and wiggler fields in an IFEL configuration (Almansa *et al.* 2019).

The work extends previous results on the acceleration of single isolated particles and examines the role of the beam density in the process.

If one initially suppresses charge densities, efficient acceleration can be reached for convenient choices of the particle's initial velocity, the wiggler and laser intensities and the phase velocity of the beat mode formed by laser and wiggler.

As the charge density of the beam increases, one would perhaps expect a detrimental effect on acceleration. What we saw, however, is that charge effects are less obvious.

In the more conventional case, where uphill acceleration effects are absent or sufficiently small, it is true that endowing the system with a non-zero charge density does indeed break

https://doi.org/10.1017/S0022377824000758 Published online by Cambridge University Press

the beam flow sooner than in the single-particle case. However, when uphill effects are present and sufficiently strong, space-charge effects actually help the forward catapulting acceleration.

We modelled the laser field as a non-expanding beam, which is an appropriate model when the radiation beam's cross-section area is large enough. It is, however, a matter of rising interest to use applications involving tightly focused radiation beams where the wave front is small and involves non-planar geometries (Singh *et al.* 2022), a topic that presents itself as a relevant extension of the present analysis.

Our analysis focuses on tenuous and sufficiently short electron beams in which the radial dynamics is moderate enough to dispense with the need for external focusing mechanisms. Higher-density beams for which factor Q_0 is larger, or even much longer beams, may require the mentioned external control (Davidson & Qin 2001), which opens yet another front where the appropriate techniques shall be added to the present line of analysis.

Acknowledgements

Editor L.O. Silva thanks the referees for their advice in evaluating this article.

Funding

We acknowledge support from CNPq, Brasil.

Declaration of interests

The authors report no conflict of interest.

Appendix A

The normalized full Hamiltonian that self-consistently describes the dynamics of an interacting particle beam with an electromagnetic field generated by a laser and wiggler can be expressed as

$$H = \sqrt{1 + (p_x - A_x)^2 + (p_y - A_y)^2 + (p_z - A_z)^2} + \varphi. \tag{A1}$$

The Hamiltonian H and the momentum components $p_{x,y,z}$ are each decomposed into two parts: the average components, symbolized by $\bar{H}$ and $\bar{p}_{x,y,z}$, and the high-frequency components, symbolized by δH and $\delta p_{x,y,z}$. Thus, we can express H and $p_{x,y,z}$ as $H = \bar{H} + \delta H$ and $p_{x,y,z} = \bar{p}_{x,y,z} + \delta p_{x,y,z}$, respectively.

To derive the average Hamiltonian component $\bar{H} = H - \delta H$, with H specified in (A1), we square this equation. We recognize the slow variations of p_y, p_z, A_x and φ, and take note that cross-terms $p_y A_y$ and $p_z A_z$ average to zero. Furthermore, we observe that the $\delta p_{y,z}$ terms are null, resulting from the Hamiltonian's independence from y and z. With these considerations, we obtain (2.11), wherein δH and δp_x are defined as follows:

$$\delta H = \int \left(\frac{\partial H}{\partial t}\right)_{\text{fast}} \mathrm{d}t, \tag{A2}$$

$$\delta p_x = -\int \left(\frac{\partial H}{\partial x}\right)_{\text{fast}} \mathrm{d}t, \tag{A3}$$

where subscript fast indicates that we are keeping only the fast quantities. Noting that we can write $A_y = A_w \cos\theta_w + A_l \cos\theta_l$ and $A_z = A_w \sin\theta_w - A_l \sin\theta_l$, where $\theta_w = k_w x$ and time appears explicitly in $\theta = x - v_\phi t$ and $\theta_l = v_\phi (x - t)$. Consequently, we have $\mathrm{d}\theta =$

https://doi.org/10.1017/S0022377824000758 Published online by Cambridge University Press

$(v_x - v_\phi)\,\mathrm{d}t$ and $\mathrm{d}\theta_l = v_\phi(v_x - 1)\,\mathrm{d}t$. While other variables might implicitly change with time, these changes are negligible on the slow time scale of our study.

Given these considerations, the variation of high-frequency Hamiltonian δH is given by

$$\delta H = \frac{A_{l0}\left(p_z \sin\theta_l + p_y \cos\theta_l\right)}{\Gamma(v_x - 1)} - \frac{v_\phi A_{l0} A_w \cos\theta}{\Gamma(v_x - v_\phi)}, \tag{A4}$$

and the variation of high-frequency momentum δp_x is defined as

$$\begin{aligned}\delta p_x = &-\frac{A_{l0} A_w \cos\theta}{\Gamma(v_x - v_\phi)} - \frac{A_w(p_y \cos\theta_w - p_z \sin\theta_w)}{\Gamma v_x} \\ &+\frac{A_{l0}(p_y \cos\theta_l + p_z \sin\theta_l)}{\Gamma(v_x - 1)},\end{aligned} \tag{A5}$$

where $\Gamma \equiv \sqrt{1 + (\bar{p}_x - A_x)^2 + \boldsymbol{p}_\perp^2 + A_{l0}^2 + A_w^2}$ and $A_w = A_{w0}\mathrm{e}^{-x^2/\sigma^2}$. Subsequently, by squaring both δH and δp_x, taking the average values and performing subtraction, we get

$$\overline{(\delta p_x)^2} - \overline{(\delta H)^2} = \delta_1 + \delta_2, \tag{A6}$$

where we define, for further purposes,

$$\delta_1 = \frac{A_{l0}^2 A_w^2 (1 - v_\phi^2)}{2(p_x - A_x - v_\phi \Gamma)^2}, \tag{A7}$$

and

$$\delta_2 = \frac{A_w^2 \boldsymbol{p}_\perp^2}{2(p_x - A_x)^2}. \tag{A8}$$

Appendix B

We can approximately write $\bar{H}$ (given by (2.11)) as the sum of two terms, H_0 and H_2, where H_0 mainly accounts for the longitudinal dynamics (we neglect the small transverse terms here) while H_2 relies on the transverse coordinates r and $\boldsymbol{p}_\perp$ to take charge of the corresponding dynamics.

To separate these terms, we introduce a 'label' to identify terms in $\bar{H}$ that depend on r and $\boldsymbol{p}_\perp$. Then, we multiply these terms by a factor ϵ without any physics significance.

Following this, a series expansion around $\epsilon = 0$ allows us to isolate these terms depending on the perpendicular direction from the rest. Finally, setting ϵ back to 1, we recover our initial Hamiltonian, now separated into the desired components.

Consequently, expanding $\bar{H}$ around $\epsilon = 0$ results in

$$\bar{H} \approx H_{\text{approx}} = \bar{H}\big|_{\epsilon=0} + \epsilon \left.\frac{\partial \bar{H}}{\partial \epsilon}\right|_{\epsilon=0} = H_0 + \epsilon H_2, \tag{B1}$$

which, assuming (2.6) to be expressed as $\varphi = \varphi_0 + \epsilon\varphi_2$, $\varphi_0 = (Q_0 v_\phi^2/4\pi v_x)(1 + 2\ln(r_w/r_b))$ and $\varphi_2 = -Q_0 v_\phi^2 r^2/4\pi v_x r_b^2$, can be expanded up to first order in ϵ as

$$\bar{H} \approx \sqrt{h_0} + \varphi_0 + \epsilon\left(\frac{h_1}{2\sqrt{h_0}} - \frac{Q_0 v_\phi^2}{4\pi v_x}\frac{r^2}{r_b^2}\right), \tag{B2}$$

https://doi.org/10.1017/S0022377824000758 Published online by Cambridge University Press

with

$$h_0 = 1 + (p_x - A_{x0})^2 + A_{l0}^2 + A_w^2 + \delta_1, \tag{B3}$$

and

$$h_1 = \boldsymbol{p}_\perp^2 + \frac{Q_0 v_\phi^2}{2\pi}(p_x - A_{x0})\frac{r^2}{r_b^2} + \delta_2, \tag{B4}$$

where the corresponding longitudinal vector potential is given by $A_{x0} = v_x\varphi_0$. Observing that we only need the equation for p_x, which arises from H_0 on the $x-$axis, then we restrict the calculation of δ_1 to the lowest order in r and yet obtain excellent agreement with the simulations, whereas δ_2 is naturally higher order due to its dependence on $p_\perp$.

Now, introducing $\Gamma_0 = \sqrt{h_0}$, then $H_0 = \Gamma_0 + \varphi_0$. Comparing (B1) and (B2) and noting that $v_x\Gamma_0 = p_x - A_{x0}$ to the lowest order, we identify the term

$$H_2 = \left(1 + \frac{\bar{A}_w^2}{2v_x^2\Gamma_0^2}\right)\frac{\boldsymbol{p}_\perp^2}{2\Gamma_0} - \frac{Q_0(1 - v_x^2)}{v_x}\frac{r^2}{r_b^2}. \tag{B5}$$

Equation (B5) is the sum of the transverse kinetic H_{2p_r} and the transverse potential energy H_{2r} expressed in (3.1). As the beam moves along its longitudinal path, the initial transverse energy converts into its kinetic form, so a good measure of the transverse energy is given by the term containing Q_0. In addition, since the thin beam aspect ratio needs the transverse energy to be smaller than the longitudinal one $\Gamma = \sqrt{1/(1 - v_x^2)}$, we thus restrict Q_0 to the range $Q_0 < \Gamma^3 v_x$.

The charge Q_0 can be large if v_x is very close to 1, but for moderate injection velocities $v_x \lesssim 1$ one must observe the more restrictive but overall safer condition $Q_0 < 1$.

REFERENCES

ALMANSA, I., BURTON, D.A., CAIRNS, R.A., MARINI, S., PETER, E., RIZZATO, F.B. & RUSSMAN, F. 2018 Uphill acceleration in a spatially modulated electrostatic field particle accelerator. *Phys. Plasmas* **25** (11), 113107.

ALMANSA, I., RUSSMAN, F.B., MARINI, S., PETER, E., DE OLIVEIRA, G.I., CAIRNS, R.A. & RIZZATO, F.B. 2019 Ponderomotive and resonant effects in the acceleration of particles by electromagnetic modes. *Phys. Plasmas* **26** (3), 033105.

BURTON, D.A., CAIRNS, R., ERSFELD, B., NOBLE, A., YOFFE, S. & JAROSZYNSKI, D. 2017 Observations on the ponderomotive force. In *Relativistic Plasma Waves and Particle Beams as Coherent and Incoherent Radiation Sources II* (ed. D. Jaroszynski). International Society for Optics and Photonics.

COURANT, E.D., PELLEGRINI, C. & ZAKOWICZ, W. 1985 High-energy inverse free-electron-laser accelerator. *Phys. Rev.* A **32**, 2813–2823.

DAVIDSON, R.C. & QIN, H. 2001 *Physics of Intense Charged Particle Beams in High Energy Accelerators*. Co-Published with World Scientific Publishing Co.

DURIS, J., MUSUMECI, P., BABZIEN, M., FEDURIN, M., KUSCHE, K., LI, R.K., MOODY, J., POGORELSKY, I., POLYANSKIY, M., ROSENZWEIG, J.B., *et al.* 2014 High-quality electron beams from a helical inverse free-electron laser accelerator. *Nat. Commun.* **5** (1), 4928.

ELMORE, W., ELMORE, W. & HEALD, M. 1985 *Physics of Waves*. Dover Books on Physics Series. Dover Publications.

EVSTATIEV, E.G., MORRISON, P.J. & HORTON, W. 2005 A relativistic beam-plasma system with electromagnetic waves. *Phys. Plasmas* **12** (7), 072108.

HO, L.V., MUSUMECI, P., DURIS, J.P. & LI, R.K. 2013 Modeling space charge effects in optical bunchers. In *Proceedings of the Particle Accelerator Conference 2013 (PAC2013)* (ed. T. Satogata, C. Petit-Jean-Genaz, & V. Schaa), p. 511. Pasadena, CA, USA.

LANDAU, L. & LIFSCHITZ, E. 1965 *Théorie du champ*. Mir.

https://doi.org/10.1017/S0022377824000758 Published online by Cambridge University Press

LONDRILLO, P., GATTI, C. & FERRARIO, M. 2014 Numerical investigation of beam-driven PWFA in quasi-nonlinear regime. *Nucl. Instrum. Meth. Phys. Res.* A **740**, 236–241, Proceedings of the first European Advanced Accelerator Concepts Workshop 2013.

MACCHI, A. 2013 *A Superintense Laser-Plasma Interaction Theory Primer*. SpringerBriefs in Physics. Springer Netherlands.

MENDONÇA, J.T. 2001 *Theory of Photon Acceleration*. Series in Plasma Physics, vol. 218. IOP Publishing.

MULSER, P. & BAUER, D. 2010 *High Power Laser-Matter Interaction*. Springer.

RUIZ, D.E. & DODIN, I.Y. 2017 Ponderomotive dynamics of waves in quasiperiodically modulated media. *Phys. Rev.* A **95** (3), 032114.

RUSSMAN, F., MARINI, S. & RIZZATO, F. 2022 A canonical view on particle acceleration by electromagnetic pulses. *J. Plasma Phys*. **88** (2), 905880204.

SHUKLA, P.K., RAO, N., YU, M. & TSINTSADZE, N. 1986 Relativistic nonlinear effects in plasmas. *Phys. Rep*. **138** (1–2), 1–149.

SINGH, J., RAJPUT, J., KANT, N. & KUMAR, S. 2022 Electron acceleration in an inverse free electron laser with a tapered wiggler field. *J. Phys.: Conf. Ser*. **2267** (1), 012068.

VAN STEENBERGEN, A., GALLARDO, J., SANDWEISS, J. & FANG, J.-M. 1996 Observation of energy gain at the BNL inverse free-electron-laser accelerator. *Phys. Rev. Lett*. **77**, 2690–2693.

VAY, J.-L. 2008 Simulation of beams or plasmas crossing at relativistic velocity[a)]. *Phys. Plasmas* **15** (5), 056701.

VRANIC, M., MARTINS, J.L., VIEIRA, J., FONSECA, R.A. & SILVA, L.O. 2014 All-optical radiation reaction at 10^{21} W cm^{-2}. *Phys. Rev. Lett*. **113**, 134801.

https://doi.org/10.1017/S0022377824000758 Published online by Cambridge University Press